Title

Meibomian gland lipid alterations and ocular surface sequela in Awat2 knockout murine model of meibomian gland dysfunction and evaporative dry eye disease.

Authors

Hisey, Erin

Wong, Sydni

Park, Sangwan

et al.

Publication Date

2024-10-01

DOI

10.1016/j.jtos.2024.10.003

Peer reviewed

HHS Public Access

Author manuscript

Ocul Surf. Author manuscript; available in PMC 2025 March 04.

Published in final edited form as:

Ocul Surf. 2024 October ; 34: 489–503. doi:10.1016/j.jtos.2024.10.003.

Meibomian gland lipid alterations and ocular surface sequela in *Awat2* knockout murine model of meibomian gland dysfunction and evaporative dry eye disease

Erin A. Hisey[a], **Sydni Wong**[a], **Sangwan Park**[a], **Kevin Aguirre Gamarra**[a], **Sara A. Adelman**[a], **Kelly E. Knickelbein**[a,b], **Melinda Quan**[a], **Michelle H. Ferneding**[a], **Michelle McCorkell**[a], **Nicole Daley**[a], **Vanessa Ureno**[a], **Sophie Le**[a], **Monica Ardon**[a], **Liana Williams**[a], **Bryan Puentes**[a], **Morgan Bowman**[a], **Monica J. Motta**[a], **Hoang Quoc Hai Pham**[c,d], **Amber Wilkerson**[c], **Seher Yuksel**[c], **James V. Jester**[e], **Sara M. Thomasy**[a,f], **Joshua T. Morgan**[g], **Igor A. Butovich**[c], **Brian C. Leonard**[a,f,*]

[a]Department of Surgical and Radiological Sciences, School of Veterinary Medicine, University of California-Davis, Davis, CA, 95616, USA

[b]Department of Clinical Sciences, College of Veterinary Medicine, Cornell University, Ithaca, NY, 14853, USA

[c]Department of Ophthalmology, University of Texas Southwestern Medical Center, Dallas, TX, 75390, USA

[d]Irell & Manella Graduate School of Biological Sciences, Beckman Research Institute, City of Hope National Medical Center, Duarte, CA, 91010, USA

[e]Department of Ophthalmology and Biomedical Engineering, University of California-Irvine, Irvine, CA, 92697, USA

[*]Corresponding author. 1275 Med Sciences Dr. Davis, CA, USA., bcleonard@ucdavis.edu (B.C. Leonard).

Declarations of interest

None.

CRediT authorship contribution statement

Erin A. Hisey: Writing – review & editing, Writing – original draft, Visualization, Validation, Methodology, Investigation, Formal analysis, Data curation, Conceptualization. **Sydni Wong:** Writing – review & editing, Validation, Investigation. **Sangwan Park:** Writing – review & editing, Investigation. **Kevin Aguirre Gamarra:** Writing – review & editing, Investigation. **Sara A. Adelman:** Writing – review & editing, Investigation. **Kelly E. Knickelbein:** Writing – review & editing, Investigation. **MelindaQuan:** Writing – review & editing, Investigation. **Michelle H. Ferneding:** Writing – review & editing, Investigation. **Michelle McCorkell:** Writing – review & editing, Investigation. **Nicole Daley:** Writing – review & editing, Investigation. **Vanessa Ureno:** Writing – review & editing, Investigation. **Sophie Le:** Writing – review & editing, Investigation. **Monica Ardon:** Writing – review & editing, Investigation. **Liana Williams:** Writing – review & editing, Investigation. **BryanPuentes:** Writing – review & editing, Investigation. **Morgan Bowman:** Writing – review & editing, Investigation. **Monica J. Motta:** Writing – review & editing, Investigation. **Hoang Quoc Hai Pham:** Writing – review & editing, Investigation. **Amber Wilkerson:** Writing – review & editing, Investigation. **Seher Yuksel:** Writing – review & editing, Investigation. **James V. Jester:** Writing – review & editing, Conceptualization. **Sara M. Thomasy:** Writing – review & editing, Supervision. **Joshua T. Morgan:** Writing – review & editing, Visualization, Validation, Software, Methodology, Formal analysis, Data curation. **Igor A. Butovich:** Writing – review & editing, Writing – original draft, Visualization, Validation, Supervision, Resources, Project administration, Methodology, Investigation, Funding acquisition, Formal analysis, Data curation. **Brian C. Leonard:** Writing – review & editing, Writing – original draft, Supervision, Resources, Project administration, Methodology, Investigation, Funding acquisition, Data curation, Conceptualization.

Appendix A. Supplementary data

Supplementary data to this article can be found online at https://doi.org/10.1016/j.jtos.2024.10.003.

[f]Department of Ophthalmology and Vision Science, School of Medicine, University of California-Davis, Davis, CA, 95616, USA

[g]Department of Bioengineering, University of California-Riverside, Riverside, CA, 92521, USA

Abstract

Purpose: There is an urgent need for animal models of meibomian gland dysfunction (MGD) and evaporative dry eye disease (EDED) to understand their pathophysiology and investigate novel therapeutics. This study sought to further define the *acyl-CoA: wax alcohol acyltransferase 2* knockout (*Awat2* KO) mouse as a model of EDED using a combination of novel clinical, biochemical, and biophysical endpoints.

Methods: Wildtype and *Awat2* KO mice between 1 and 18 months of age were used. Ocular examinations and advanced imaging were performed. The lipidomic composition and *in situ* melting temperature of meibum were determined. qPCR was performed to define ocular surface gene and pro-inflammatory transcript expression. Dynamic contact angle goniometry was performed to assess the adherence capability of the ocular surface.

Results: *Awat2* KO mice have mild, white, hyperreflective corneal opacities of the anterior stroma and significantly enlarged apical epithelial cells ($P = 0.0004$). In *Awat2* KO meibum, wax esters were 9–10 times lower than in wildtype meibum. Additionally, meibum melting temperature increased from 32° to 47 °C ($P < 0.0001$), leading to impaired meibum secretion and dilation of the central duct. *Awat2* KO corneal epithelia had significantly decreased mucin expression (*Muc1* and *Muc4*, $P = 0.0043$) and increased interferon-γ production ($P = 0.0303$). *Awat2* KO globes have a significantly shortened time of droplet adherence to their ocular surface ($P = 0.0053$), indicating a decreased tear film adherence capacity. Wildtype corneal epithelia does not express *Awat2*, indicating that the EDED phenotype is secondary to the loss of *Awat2* from the meibomian glands.

Conclusions: *Awat2* KO mice recapitulate many of features of human MGD and EDED, representing a model to test novel therapeutics.

Keywords

Dynamic contact angle goniometry; Evaporative dry eye disease; Heat stage cross-polarized light microscopy; *In vivo* confocal microscopy; Meibomian gland dysfunction; Meibomian gland inspissation; Mouse models of dry eye disease; Optical coherence tomography

1. Introduction

Dry eye disease (DED) is an ophthalmic disorder defined by a loss of tear film homeostasis leading to subsequent ocular surface inflammation and irritation [1]. There are two main subtypes of DED: aqueous deficient dry eye (ADDE) and evaporative dry eye disease (EDED) with the evaporative form being more common clinically [2,3]. In EDED, decreased tear film stability is typically due to deficiencies in the tear film lipid layer [2]. Since the tear film lipid layer is predominantly synthesized by the meibomian glands, meibomian gland dysfunction (MGD) is a leading causes of EDED. MGD is a multifactorial condition in which acinar atrophy and/or senescence, seen clinically as meibomian gland

dropout, leads to reduced and/or altered lipid production [2,4]. Alternatively, primary alterations in lipid production can obstruct the central duct of the meibomian gland leading to impaired lipid secretion [5]. Other than increasing fluidity of the lipids from the meibomian glands either via heat or light therapy [6,7], the majority of current FDA-approved therapeutics for DED, such as immunomodulation and tear replacement [8], do not target the mechanism(s) of disease in patients with EDED and thus only provide palliative benefit. A new treatment, Miebo, was recently approved as a topical treatment for EDED that can prevent evaporation of the tear film by coating the ocular surface with an organic solution [9]. However, this solution would still need to be applied multiple times per day and can alter vision [9,10]. Thus, the development of novel mechanism-derived therapeutics is still necessary.

Early models of MGD focused on gland obstruction caused by hyperkeratinization of the meibomian gland duct (i.e. treatment of rabbits with topical epinephrine [11], treatment of monkeys with polychlorinated biphenyl [12], the Rhino mouse [13], etc.), induced glandular atrophy (treatment with Accutane) [14], or altered meibomian gland development through alterations in growth hormone activity [15]. Additional murine models of MGD consist of feeding hairless mice a lipid deficient diet [16] and treatment with isotretinoin [17], a known human MGD risk factor. However, the relevance of these models to MGD and secondary EDED are unclear. More recent models include the creation of genetic knockouts that alter the synthesis of meibomian gland lipids leading to altered meibum lipid quality and inducing meibomian gland obstruction that is seen in human patients [18–22]. One of these new models is the *acyl-CoA: wax alcohol acyltransferase* knockout (*Awat2* KO) mouse [23,24]. AWAT2 is a key enzyme in the synthesis of long-chain wax esters in the meibomian gland. As wax esters make up approximately 43 % of the human tear film lipids and they are dysregulated in patients with MGD [25,26], the use of the *Awat2* KO mouse model to study EDED is promising. However, the impact of a deficiency in long-chain wax esters synthesis on ocular surface health remains poorly understood.

This study aimed to further explore the consequences of the loss of *Awat2* on meibomian gland lipid quality and ocular surface health, and to better characterize this model for future studies investigating novel mechanism-derived therapeutics for MGD and EDED. Eyelids were collected for qPCR, histopathology, lipidomics and meibum melting point using lipid birefringence to assess meibomian gland health and function. We hypothesized that *Awat2* KO mice would show overt clinical signs of EDED by six months of age with severity increasing over time, thus clinical examinations and imaging were performed at six months of age and the progression of disease was investigated with additional endpoints, like histopathology and dynamic contact angle goniometry, using globes from older mice. Additionally, dynamic contact angle goniometry was performed on whole globes and RNA was isolated from the corneal epithelium to determine the impact of a deficiency in long-chain wax ester synthesis on ocular surface health. Together, these findings provide further support for the use of *Awat2* KO mice as a preclinical model of human EDED.

2. Methods

2.1. Murine model generation

To generate *Awat2* KO mice, the University of California, Davis (UCD) Mutant Mouse Resource and Research Centers (MMRRC) utilized the CRISPR/Cas9 system to splice exon 3 of *Awat2* and its flanking sequence from murine zygotes (C57BL/6NCrl). Heterozygous females (*Awat2*$^{+/-}$), homozygous females (*Awat2*$^{-/-}$) and hemizygous males (*Awat2*$^{-/y}$) were acquired from the MMRRC which were utilized to establish a breeding colony. Animal experiments were performed in strict accordance with the Association for Research in Vision and Ophthalmology Statement for the Use of Animals in Ophthalmic and Vision Research and the ARRIVE guidelines and with approval by the UCD Animal Care and Use Committee (21825). Approximately equal numbers of males and females were used in all experiments.

2.2. Mouse genotyping

Tail tips and/or ear punches were obtained from all mice and DNA was extracted using the QIAmp DNA Mini Kit (Qiagen, Hilden, Germany). Genotyping PCR was performed using the MyTaq HS Red Mix (Meridian Bioscience, Cincinnati, OH) using primers designed by the UCD Mouse Biology Program (Supplemental Table 1). PCR conditions were as follows: 95 °C for 1 min; 95 °C for 15 s, 64 °C for 15 s, 72 °C for 1 min, repeat 35X; 72 °C for 7 min. Amplicon size was assessed using a precast agarose E-gel with SYBR safe gel stain (ThermoFisher Scientific, Waltham, MA). Sanger sequencing was performed to verify amplicon identity as described previously [27].

2.3. Clinical examinations and disease scoring

As a previous report identified increased corneal damage scores in 23 week old *Awat2* KO mice [24], complete anterior segment ophthalmic examinations including fluorescein staining (I-GLO fluorescein sodium ophthalmic strips, Jor-Vet, Loveland, CO) were performed on six-month-old *Awat2* KO (n = 13) and WT (n = 6) mice by a board-certified veterinary ophthalmologist (BCL). Examinations were performed using a handheld slit lamp biomicroscope (SL-17; Kowa American Corp., Torrance, CA). Additionally, digital slit lamp biomicroscopy imaging (Haag-Streit B 900 Slit Lamp, Köniz, Switzerland) was performed to capture the adnexa and anterior segment (n = 26 KO, n = 15 WT). The mice were sedated with ketamine (50–75 mg/kg) and dexmedetomidine (100–375 μg/m^2) for imaging. Eyes were dilated with 1 % tropicamide to facilitate adequate imaging of the ocular surface pathology against a black background (dilated pupil).

Clinical findings were scored using the Semiquantitative Preclinical Ocular Toxicology Scoring (SPOTS) system [28], a validated scoring rubric for adverse ophthalmic events. Only the conjunctival/ocular discharge, which was used to denote the clogged meibomian gland orifices as there is no direct measure of meibomian gland inspissation in this scoring system, corneal opacity severity and corneal opacity area data from the SPOTS assessment are presented here as the other parameters were consistent across genotypes. Additionally, phenol red thread tests (PRTT) were performed on awake animals to determine tear production of two-month-old *Awat2* KO (n = 6) and WT (n = 10) mice. Forceps were

utilized to place the end of the thread (Zone-Quick, Menicon America Inc., San Mateo, CA) under the lower eyelid adjacent to the lateral canthus for 15 s and the color change was measured with digital calipers. This procedure was repeated multiple times to ensure the reproducibility of results with at least 24 h between measurements as described previously [29].

2.4. qPCR

After sedation as described above, mice were euthanized with intraperitoneal sodium pentobarbital injection (<100 mg/kg). Eyelids (*Awat2* KO n = 5, WT n = 6, 1- to 18-months-old to investigate a spectrum of ages) were carefully removed, submerged in RNAlater and stored at −20 °C until total RNA was extracted using the GeneJET RNA Purification Kit (ThermoFisher Scientific) as described previously [27]. The corneal epithelium (*Awat2* KO n = 5, WT n = 6, 3- to 16-months-old to investigate differing degrees of chronicity) was debrided with a #15 scalpel blade using a surgical microscope (OPMI-6-SFC Universal S3 ENT Microscope, Zeiss, Jena, Germany) and RNA was isolated using the GeneJET RNA Purification Kit (ThermoFisher Scientific). RNA yield was quantified using a Nanodrop spectrophotometer and treated with dsDNase (ThermoFisher Scientific) to remove residual genomic DNA. A final RNA concentration of approximately 30 ng/μL for the eyelid samples and 5–20 ng/μL for the corneal epithelial samples was achieved. Commercial aptamers for *Gapdh* (Mm99999915_g1, ThermoFisher Scientific) and *Awat2* (Mm01232856_g1) were used to assessed the *Awat2* expression in eyelid and corneal epithelial samples using the SensiFAST Probe Hi-ROX One-Step Kit (Life Technologies, Carlsbad, CA). Amplification was performed using the StepOne Real-Time PCR System (Life Technologies) with the following parameters: 50 °C for 30 min, 95 °C for 10 min followed by 40 cycles of 95 °C for 15 s and 68 °C for 1 min in triplicate. Additionally, the corneal epithelium of four-month-old *Awat2* KO (n = 6) and WT (n = 5) mice were assessed for corneal epithelial and inflammatory markers including *mucin 1* (*Muc1*, Mm00449604_m1), *Muc4* (Mm00466886_m1), *interferon gamma* (*Ifn-γ*, Mm01168134_m1) and *interleukin 1 beta* (*Il-1β*, Mm00434228_m1) using commercially available aptamers. Amplification was performed using the TaqPath 1-Step RT-qPCR Master Mix (ThermoFisher Scientific) and the QuantStudio3 (ThermoFisher Scientific) in duplicate with 10–25 ng RNA using the following parameters: 50 °C for 30 min, 95 °C for 10 min followed by 40 cycles of 95 °C for 15 s and 60 °C for 1 min. Relative expression was determined using the $2^{-\Delta Ct}$ method [30].

2.5. Histopathology

As a mild clinical phenotype was identified in the six-month-old mice, histopathological assessment was performed on tissues from animals with a more advanced age to assess the potential for disease progression. Eyelids (n = 22 *Awat2* KO and n = 5 WT, 9-month-old; n = 8 *Awat2* KO and n = 5 WT, 18-month-old) and enucleated globes (n = 15 *Awat2* KO and n = 5 WT, 9-month-old; n = 8 *Awat2* KO and n = 5 WT, 18-month-old) were placed in tissue cassettes and submerged in 4 % paraformaldehyde for 24–48 h. After fixation, tissues were paraffin embedded, sectioned, and stained with hematoxylin and eosin (H&E). Additional eyelid sections were stained with periodic acid-Schiff to assess conjunctival goblet cell density.

Custom MATLAB algorithms (2020A; Mathworks, Natick, MA) were used to quantify the corneal epithelial thickness of the H&E histological sections. Briefly, RGB images of the H&E sections were deconvolved to separate the respective histological stains [31]. The epithelium was segmented as a region of interest from the eosin channel using K-means clustering [32]. The centerline of the epithelial region of interest was determined using a modification of the fast marching skeletonization algorithm described by van Uitert and Bittner 2007 [33], allowing quantification of the epithelial thickness at all points along the section.

2.6. Lipidomics

Meibum was collected from four-month-old *Awat2* KO (n = 7) and WT (n = 8) mice to assess the meibum lipid alterations in adult animals before any potential age-related changes to meibum lipid expression could occur. The lipids were identified as described previously [34]. Briefly, the individual meibomian lipid samples were dissolved in 1 mL of 2-propanol and stored at −80 °C in 2 mL glass autoinjector vials sealed with PTFE-lined caps. The lipidomic analyses were performed using ultra-high performance liquid chromatography (UPLC) high resolution mass spectrometry (HRMS) and analyzed in atmospheric pressure chemical ionization positive ion mode (APCI PIM). The analyses were performed using a Waters Acquity M-Class UPLC system coupled to a Synapt G2-Si high resolution Time-of-Flight (ToF) mass spectrometer (Waters Corp., Milford, MA). Then, untargeted, unbiased lipidomic analyses of *Awat2* KO and WT meibum samples were conducted as described before [34]. The raw UPLC-HRMS data were initially processed in the Progenesis QI software package (version 2.3; Nonlinear Dynamics/Waters Corp., Milford, MA), then exported into the EZInfo software (v3.0.3; from Umetrics/Waters Corp., Milford, MA) and analyzed using its OPLS-DA algorithm (a package within the EZInfo software). The most statistically significant and influential lipids that differed between the two groups were determined using the S-Plot.

2.7. Lipid birefringence

Under polarized light, meibum lipids show a distinct birefringence pattern and changes in these patterns can be utilized to determine their melting point [34,35]. Melting points of the meibum from *Awat2* KO (n = 3) and WT (n = 3) eyelids were determined as described previously using heat stage cross-polarized light microscopy [35].

2.8. Advanced imaging

To further characterize the clinical phenotype of the six-month-old mice, advanced imaging was utilized. Spectral-domain optical coherence tomography (SD-OCT; RTVue 100, Optovue, Fremont, CA) was performed on *Awat2* KO (n = 26) and WT (n = 14) mice to evaluate the structural organization of the cornea. Central corneal, epithelial, and stromal thickness were measured on horizontal and vertical images using the RTVUE software (version 6.8) by a grader masked to animal genotype. Horizontal and vertical measurements from the same eye were averaged for each layer for analysis. *In vivo* confocal microscopy (IVCM) was performed using a Heidelberg Retinal Tomography 3 in conjunction with the Rostock Cornea Module (Heidelberg Engineering, Heidelberg, Germany) to assess corneal cell morphology of *Awat2* KO (n = 11) and WT (n = 13) mice. Apical epithelial cell area

was determined using ImageJ by averaging the measured areas of 5–7 cells per eye from a single image (*Awat2* KO n = 17 images, WT n = 23 images). Basal epithelial cell density was determined via manual counts using the Heidelberg Eye Explorer software (version 1.10.4) by a grader masked to genotype (*Awat2* KO n = 19 images, WT n = 17 images).

2.9. Dynamic contact angle goniometry

In health, the corneal epithelial glycocalyx contributes to the adherence of the tear film to the corneal surface [2]. Patients with EDED can have an altered or ablated corneal glycocalyx and therefore decreased adherence of their tear film to the ocular surface, which can exacerbate their DED phenotype [2]. A previous study identified a severe ocular surface phenotype in 12-month-old Awat2 KO mice [23], thus 12-month-old *Awat2* KO (n = 10) and WT (n = 11) globes were used to assess the health of the corneal epithelium by determining its adherence capacity. Specifically, the globes were enucleated, rinsed in phosphate buffered saline (PBS), and mounted on glass slides using cyanoacrylate adhesive gel and oriented with the axial cornea facing upright, using a dissecting microscope. Prepared slides were submerged in PBS. For analysis, the slides were secured in the dynamic contact angle goniometer stage (Ramé-Hart Instruments, Succasunna, NJ) and submerged in an environmental chamber filled with PBS. A five μL droplet of perfluorodecalin (Sigma-Aldrich, St. Louis, MO) was placed on the axial cornea using an automated pipette [36]. As the stage was tilted (0.5°/sec), a video recording was taken of the droplet deforming and rolling off the ocular surface. The experiment was repeated three times for each globe. Dynamic contact angle goniometry measurements were taken within 3 h of euthanasia. The videos were analyzed using a custom MATLAB script (Mathworks). Briefly, initial segmentation of the globe and droplet for each frame was conducted with hysteresis-based thresholding, similar to previous studies [37]. The boundary pixels were rendered as a curve and tracked until the droplet was liberated from the ocular surface, allowing automated identification of the globe/droplet/PBS junction as peak curvature. The interface angles were automatically extracted using linear fits to short segments bracketing the junction. These measurements were used to identify the $\cos \theta_{\text{advancing angle}}$ (the angle at the front) and the $\cos \theta_{\text{receding angle}}$ (the angle at the back) of the droplet. The difference between these angles was the hysteresis value. The duration of droplet contact on the ocular surface and the tilt of the dynamic contact angle goniometer were also determined. The average values from the three videos were utilized for statistical analysis.

2.10. Statistical analysis

The normality of the SPOTS and qPCR data were assessed using a Kolmogorov-Smirnov normality test. A Shapiro-Wilk test for normality was performed on all remaining datasets. Results from the *Awat2* KO and WT mice were compared using a Mann-Whitney test for the SPOTS scoring, PRTT measurements, qPCR data, and OCT and histopathologic epithelial thickness measurements, and a student's *t*-test for to compare the lipid relative abundance, meibum melting temperature, and IVCM and dynamic contact angle goniometry measurements. Outliers for the normally distributed data were determined if they were outside the range of the mean ±2 times the standard deviation and outliers for the nonparametric data were determined if they were less than the 25th percentile minus 1.5 times the interquartile range or greater than the 75th percentile plus 1.5 times the

interquartile range. Outliers were excluded from the statistical testing. Analyses were performed using GraphPad Prism (version 9.5.1).

3. Results

3.1. Clinical examinations and diagnostics

Dense, white, inspissated meibum that protruded from the meibomian gland orifices was observed in the *Awat2* KO mice, which resulted in the obstruction and dilation of the meibomian gland (Fig. 1). White fragments of inspissated meibum could be found throughout the lackluster tear film that covered the corneal surface (Fig. 1C and D). Anterior segment slit lamp biomicroscopy revealed mild to moderately dense, horizontally oriented oval shaped corneal opacities located within the interpalpebral fissure in the Awat2 KO mice that were not observed in the WT mice (Fig. 1). The conjunctival discharge (as a proxy for the meibum adherence to the eyelid margin, Fig. 2A), corneal opacity severity (Fig. 2B) and corneal opacity area (Fig. 2C) scores were significantly increased in the *Awat2* KO mice compared to the WT mice (Mann-Whitney, $P < 0.0001$). Additionally, there was a significant increase in PRTT (aqueous tear production) in the *Awat2* KO mice compared to the WT mice (Mann-Whitney, $P = 0.0098$, Fig. 2D). The PRTT data shown here were also presented in a recently published manuscript as controls for the development of an in house PRTT [29].

3.2. Meibomian glands

3.2.1. qPCR—A qPCR analysis of eyelid samples identified *Awat2* gene expression in all WT andno *Awat2* KO samples. The $2^{-\Delta Ct}$ values between the *Awat2* KO and WT mice were compared, which identified a significant decrease in *Awat2* expression in the KO eyelid tissue (Mann-Whitney, $P = 0.0043$, Fig. 3).

3.2.2. Meibomian gland histopathology—Histological evaluation of the meibomian glands identified ductal epithelial hyperplasia and dilation of the central ducts and their associated orifices at the eyelid margins in the *Awat2* KO mice (Fig. 4). Inflammatory cell infiltration was identified in the lumen and adjacent to the ducts of a small portion of the *Awat2* KO meibomian glands (Fig. 4C). Goblet cell hyperplasia was identified in the palpebral conjunctiva overlying the meibomian glands in the *Awat2* KO eyelids (Fig. 4D), but not in the WT eyelids.

3.2.3. Lipidomics—The representative observation LC-MS spectra of WT and *Awat2* KO meibum samples are shown in Fig. 5A–D. The results were highly reproducible with no noticeable differences between animals of the same genotype as the WT and *Awat2* KO samples formed two tight groups in the OPLS-DA analysis with rather low intra-group differences, while large differences between the WT and *Awat2* KO meibum were observed (Fig. 5E). The main differences between the WT and *Awat2* KO meibum were in the abundance of three major wax esters, shown in the lower left quadrant of the S-Plot, and a combined pool of cholesteryl esters in the upper right quadrant (Fig. 5F).

A more targeted and quantitative lipidomic analysis confirmed a severe decrease of the wax esters and a concomitant increase in the cholesteryl ester and free cholesterol content of the *Awat2* KO meibum. Due to a large number of individual species of wax esters, their total amount was not estimated. However, when the apparent abundance of the primary meibomian wax ester (m/z = 619.6417) was assessed, it was decreased 9–10-fold in the *Awat2* KO meibum. The abundance of two other major wax esters (m/z = 633.6538 and 647.6725) were also compared, which identified a significantly decreased abundance in all three species in the *Awat2* KO meibum (t-test, $P < 0.001$).

3.2.4. Lipid birefringence—Assessment of *Awat2* KO and WT eyelids utilizing lipid birefringence revealed that *Awat2* KO mice had an increased meibum melting temperature compared to the WT controls (Fig. 6). The main transition temperatures (T_m) of both samples were determined after numeric differentiation of their melting curves as shown in Fig. 6C. While the WT meibum had a major transition temperature of around 32 °C (305 K), the *Awat2* KO meibum melted around 47 °C (320 K) indicating that at physiological temperatures, the wildtype meibum was partially melted whereas the *Awat2* KO meibum was almost completely solid. The melting temperature of the *Awat2* KO meibum was significantly increased compared to the WT meibum (t-test, $P < 0.0001$).

3.3. Ocular surface

3.3.1. Advanced imaging—OCT image analysis identified hyperreflective lesions present in the anterior stroma of the *Awat2* KO mice that was consistent with the corneal opacities identified on slit lamp biomicroscopy (Fig. 7A and B). A Mann-Whitney test was utilized to compare the WT and the *Awat2* KO OCT measurements, which identified no significant differences between the central corneal ($P = 0.9980$, Fig. 7C), epithelial ($P = 0.4662$, Fig. 7D) or stromal thicknesses ($P = 0.5183$, Fig. 7E).

IVCM image analysis revealed large, hyperreflective apical epithelial cells with larger dark spaces between the cells in the *Awat2* KO mice compared to the WT mice (Fig. 8A and B). The mean area of the apical epithelial cells was quantified and identified to be significantly larger in the *Awat2* KO mice (student's t-test, $P < 0.0001$, Fig. 8C). Additionally, there was a trend towards an increase in basal epithelial cell density in the *Awat2* KO mice (student's t-test, $P = 0.0693$, Fig. 8D–F).

3.3.2. qPCR—In the corneal epithelium, very low and highly variable *Awat2* gene expression was identified in the WT samples and no detectable expression was identified in the *Awat2* KO samples, which was a significantly reduction compared to the WT samples (Mann-Whitney, $P = 0.0043$, Fig. 3). Additionally, *Awat2* expression was significantly lower in the WT corneal epithelial tissue compared with the eyelid samples (Mann-Whitney, $P = 0.0022$, Fig. 3).

To evaluate the cellular consequences of a tear film devoid of long-chain wax esters on the ocular surface, we performed a qPCR analysis for commonly expressed corneal epithelial genes in health and proinflammatory cytokines that are upregulated in the tears of human patients with DED. This analysis identified a significant decrease in *Muc1* (Mann-Whitney, $P = 0.0043$, Fig. 9A) and *Muc4* ($P = 0.0043$, Fig. 9B) expression, and a significant increase

in *Ifn-γ* expression ($P = 0.0303$, Fig. 9C), but no difference in expression of *Il-1β* ($P = 0.5368$, Fig. 9D) in *Awat2* KO mice.

3.3.3. Ocular surface histopathology—Histological evaluation identified similar pathology in the *Awat2* KO corneas between both the 9- and 18-month age groups, which contrasted with the WT mice, which showed no corneal pathology at either age (Fig. 10). The *Awat2* KO corneas consistently exhibited mild corneal pathology with a majority of sections (18 of 30 sections) demonstrating a hypereosinophilic anterior stroma (Fig. 10C and D), but relatively few showed degeneration (Fig. 10E) or disorganization (Fig. 10F) of their corneal epithelium or had basophilic subepithelial basophilic deposits (Fig. 10G and H). A trend towards a significant decrease in corneal epithelial thickness was identified in the 9-month-old *Awat2* KO corneas (Mann-Whitney, $P = 0.0655$, Fig. 10I), whereas in the 18-month-old group, a significant decrease in epithelial thickness was identified in the *Awat2* KO corneal epithelium (Mann-Whitney, $P = 0.0012$, Fig. 10J).

3.3.4. Dynamic contact angle goniometry—Dynamic contact angle goniometry was utilized to determine the adherence capacity of the corneal surface. Prior to droplet placement, corneal lesions were identified on half of the *Awat2* KO globes (n = 5) assessed compared to no lesions on the WT globes (Fig. 11A and B, Supplemental Video 1–2). A significant decrease in the duration of droplet contact was seen for the *Awat2* KO globes compared to the WT globes (student's *t*-test, $P = 0.0053$, Fig. 11C) and the final tilt angle of the system was decreased for the *Awat2* KO globes compared to WT globes (student's *t*-test, $P = 0.0072$, Fig. 11D). Additionally, the advancing angle, or the angle at the front of the droplet, and the hysteresis values were significantly decreased in the *Awat2* KO globes (student's *t*-test, $P = 0.0299$ and 0.0331, respectively, Fig. 11), A trend towards a significant increase in the receding angle was identified in the *Awat2* KO globes (student's *t*-test, $P = 0.0637$, Fig. 11F).

Supplementary video related to this article can be found at https://doi.org/10.1016/j.jtos.2024.10.003

4. Discussion

This study characterized the anatomical and functional consequences of an abnormal tear film devoid of long-chain wax esters on the meibomian glands and ocular surface. The altered meibum lipid composition of the *Awat2* KO mice leads to an increase in meibum melting temperature, causing marked meibomian gland inspissation, and preventing lipid secretion seen both on clinical and histological examinations. Mice with this abnormal tear film developed white, hyperreflective corneal opacities in their anterior stroma, hyperreflective apical corneal epithelial cells, reduced expression of corneal mucins and increased expression of pro-inflammatory cytokines. These changes corresponded with mild histological changes including epithelial thinning and a decreased ability to adhere a droplet to the ocular surface. As expression of the *Awat2* gene was not detected in the corneal epithelium of WT mice, the ocular surface pathology seen in the *Awat2* KO mice are the direct result of the abnormal lipid composition from the meibomian glands and subsequent

alterations in the tear film, supporting their utility as a murine model of EDED secondary to MGD.

The presence of the corneal epithelial glycocalyx converts the inherently hydrophobic corneal epithelium into a hydrophilic surface, thus the glycocalyx increases the wettability of the corneal epithelium, or the ability of the aqueous tear components to interact with the corneal surface [2]. The corneal epithelial cells of patients with EDED have been shown to have a loss of the normal corneal glycocalyx, particularly the mucins [28,38], leading to decreased adherence of the tear film to the cornea which exacerbates the EDED [2]. Measuring the wettability of the corneal surface *in vivo* is challenging, but our laboratory adapted a method called dynamic tilt contact angle goniometry to investigate the impact of EDED on the wettability of the corneal surface of the *Awat2* KO mice *ex vivo*. Our results indicate that the ocular surface of mice with EDED has an impaired ability to adhere to a droplet, indicating that their ocular surfaces would have both a decreased wettability and adherence to the tear film. Our laboratory has previously shown that the presence of ocular surface mucins play a major role in the ability of a droplet to adhere to corneal epithelial cells *in vitro* [36]. Here, we identified that the *Awat2* KO corneal epithelium has a decreased expression of *Muc1* and *Muc4*, a change that is also found in humans with DED [38,39]. Thus, this lack of ocular surface mucins could further exacerbate the EDED phenotype in these mice due to an inability to maintain tear film adherence, leading to the vicious cycle of inflammation that is characteristic of DED [2]. Additionally, these results suggest that duration of droplet contact, final tilt angle, advancing/receding angle and hysteresis could be parameters measured in *ex vivo* animal models as a functional marker. Overall, these results indicate that dynamic contact angle goniometry is a valuable tool to determine differences in adherence capabilities of the ocular surface.

Clinically, the *Awat2* KO mice have meibum obstructed meibomian glands, suggesting that this meibum that cannot be physically expressed onto the ocular surface to contribute to the tear film. We confirmed that the melting temperature of *Awat2* KO meibum was significantly higher than that of WT mice, suggesting that the increase in meibum melting point above body temperature causes thermodynamic alterations in the lipids, interfering with the secretion of meibum and causing gland obstruction and ductal dilation. Importantly, these mice recapitulate the altered meibum lipid composition, and increased meibum melting temperature of human patients with MGD [26,35,40]. Interestingly, a similar increase in meibum melting temperature was recently identified in the *Soat1* (*sterol O-acyltransferase 1*) KO mice as their meibum melting temperature increased to over 50 °C compared to 34 °C in WT meibum [34]. In contrast to the wax ester deficiency seen in the *Awat2* KO mice, meibum from the *Soat1* KO mice have a deficiency in cholesteryl esters, the other predominant class of nonpolar lipids in the tear film, leading to a compensatory increase in free cholesterol in their meibum [34]. Together, these results suggest that any dysregulation of the meibum lipid composition alters the interactions between meibum lipids, causing an increase in melting temperature that prevents the excretion of these lipids onto the ocular surface.

Two prior publications utilizing *Awat2* KO mice identified similar meibomian gland obstruction and alterations in the *Awat2* KO meibum to what was seen here [23,24].

Specifically, Widjaja et al., 2020 identified a significant decrease in wax ester and a significant increase in cholesteryl ester abundance in the *Awat2* KO meibum compared to WT meibum [23]. Sawai et al., 2021 also identified a significant decrease in several species of wax ester compared to WT meibum [24]. We have also described similar alterations here with the *Awat2* KO mouse meibum being composed largely of free cholesterol, cholesteryl esters, and triacylglycerols, with minor amounts of other acylglycerols [41].

Importantly, the *Awat2* KO mouse described in this study seems to better recapitulate many of the features of moderate to advanced MGD and EDED in humans due to its less severe ocular surface phenotype [23]. Widjaja et al., 2020 described ulceration, marked corneal thickening, and neovascularization of the ocular surface in their *Awat2* KO model, indicating severe ocular surface disease [23]. The mice in the current study generally appeared to have a milder ocular surface phenotype characterized by small, white, hyperreflective anterior stromal corneal opacities without an increase in corneal thickness seen on clinical examination and with OCT imaging as well as hyperreflective apical corneal epithelial cells. However, these differences in disease severity could be attributed to environmental or strain-specific factors as they both had a functional loss of AWAT2. As humans with MGD typically present with mild corneal pathologies, if any, the *Awat2* KO model detailed in the current study may better recapitulate the disease seen in humans with EDED.

Additionally, we identified an increase in *Ifn-γ* gene expression from the corneal epithelium of *Awat2* KO mice, a finding that recapitulates the upregulation of IFN-γ seen in humans with EDED [2,42,43]. In humans, increased expression of IFN-γ leads to squamous metaplasia of the corneal epithelial cells [44] and decreased functionality of the apical epithelium, thus perpetuating the dry eye phenotype. In this study, we identified that apical corneal epithelial cells of these mice were abnormally hyperreflective, the corneal epithelium had altered mucin expression, and the ocular surface had an impaired ability to adhere to a droplet, indicating a decreased functionality of the corneal epithelium. Thus, these findings provide further support for the use of the *Awat2* KO mice as a model for human EDED.

These similarities suggest that this *Awat2* KO model could potentially be utilized to better understand the pathologic events occurring in human patients with EDED. Specifically, we identified larger apical corneal epithelial cells suggesting that there is an increase in corneal epithelial cell turnover and compensatory cellular hypertrophy as a response to the chronic corneal epithelial injury due to the abnormal tear film of the *Awat2* KO mice. Similarly, in human patients with Sjögren's disease, one of the main causes of ADDE, an increase in superficial corneal epithelial cell area was identified [45]. This study also identified a trend towards lowered basal cell density as was seen here in the *Awat2* KO mice [45]. The identification of these cellular changes in the *Awat2* mice indicate that epithelial turnover should be an area of future study using this murine model.

The *Awat2* KO mouse model generally recapitulates the clinical disease seen in human patients with MGD and EDED, but there have been no mutations in *Awat2* identified to date that have been associated with MGD/EDED in humans. Thus, the few phenotypic differences between the *Awat2* KO mouse model and humans with MGD and EDED could

be unique to this genetic deficiency and the specific responses to the loss of *Awat2*. For example, the *Awat2* KO mice exhibited an increase in conjunctival goblet cells, which differs from human patients with EDED as they have been found to have a decrease in conjunctival goblet cells [46,47]. In humans, this loss of goblet cells is typically attributed to goblet cell apoptosis due to the hyperosmolar tear film and the presence of proinflammatory cytokines, such as IL-1β, in the tear film [2]. This study identified that the *Awat2* KO corneal epithelium did not have an increased expression of *Il-1β*, which could potentially enable this goblet cell proliferation. As conjunctival goblet cells secrete MUC5AC, a mucin that increases the viscosity of the tear film and provides lubrication to the lid and globe [2,48,49], this could represent a compensatory mechanism to combat the loss of tear film stability from the altered lipids of the *Awat2* KO tear film. Additionally, the loss of AWAT2 expression and subsequent decrease in wax ester synthesis causes the cholesteryl ester to wax ester ratio to increase in the *Awat2* KO mice, which contrasts with the results from meibum from humans with MGD which shows an decrease in the cholesteryl ester to wax ester ratio [50, 51]. However, despite these differences, the *Awat2* KO mouse represents a promising model for the human condition as it exemplifies the main clinical features of human patients with MGD and EDED.

5. Conclusions and future directions

The *Awat2* KO mice described here have clinical signs that recapitulate the pathology seen in patients with moderate to severe MGD and EDED. The *Awat2* KO mice have clinically apparent meibomian gland obstruction, mild to moderately dense corneal opacities, hyperreflective apical epithelial cells and anterior stroma consistent with advanced ocular surface disease. The meibum lipidomic analysis identified altered production of the meibum cholesteryl and wax esters. These alterations increase the meibum melting temperature, suggesting that the meibomian gland obstruction is due to a decreased ability to secrete the meibum lipids onto the ocular surface. Additionally, these mice exhibit a decreased ability to adhere a droplet to their ocular surface along with altered mucin and inflammatory cytokine expression. Together, these results demonstrate that the *Awat2* KOmice have phenotypic similarities to patients with EDED secondary to MGD and that this *Awat2* KO mouse model could be utilized to study the pathogenesis of EDED and MGD and to investigate novel, mechanism-derived therapeutics.

Supplementary Material

Refer to Web version on PubMed Central for supplementary material.

Acknowledgments

The authors would like to thank Bradley Shibata and the UCD, School of Veterinary Medicine Anatomic Pathology Department for their technical assistance. The authors would also like to acknowledge Drs. Tom Glaser and Paul Russell for their contributions to the study design.

Funding

This work was supported by UCD School of Veterinary Medicine, the UCD School of Medicine and Department of Ophthalmology & Vision Science Claire Burns Audacious Grant (VMSPBAG), and by the NEI core grant P30EY12576. Financial support for EAH was provided by the MSTP T32 (GM136559), NEI T32 (EY015387),

NEI F30 (EY035132) and Maxine Adler Fellowship, for BP was provided by the UCD Students Training in Advanced Research (STAR) Program through the NIH (T35-OD010956), for SMT by the NEI R01 (EY016134), for IAB by the NEI R01 (EY027349), and for BCL by the NEI K08 (EY028199). The funding sources were not involved in the study design, collection, analysis and interpretation of the data, in writing the report, or in the decision to submit this article for publication.

Data availability

The data associated with this manuscript are available from the corresponding author upon reasonable request.

Abbreviations:

ADDE	aqueous deficient dry eye disease
APCI PIM	atmospheric pressure chemical ionization positive ion mode
Awat2	acyl-CoA, wax alcohol acyltransferase 2
DED	dry eye disease
EDED	evaporative dry eye disease
Gapdh	Glyceraldehyde 3-phosphate dehydrogenase
H&E	hematoxylin and eosin
HRMS	high resolution mass spectrometry
Ifn-γ	interferon gamma
Il-1β	interleukin-1 beta
IVCM	*In vivo* confocal microscopy
KO	knockout
m/z	mass-to-charge ratio
MGD	meibomian gland dysfunction
MMRRC	Mutant Mouse Resource and Research Centers
Muc	mucin
PRTT	phenol red thread test
PTFE	Polytetrafluoroethylene
SD-OCT	Spectral-domain optical coherence tomography
Soat1	sterol O-acyltransferase 1
SPOTS	Semiquantitative Preclinical Ocular Toxicology Scoring
T_m	main transition temperature

ToF	Time-of-Flight
UCD	University of California, Davis
UPLC	ultra-high performance liquid chromatography
WT	wildtype

References

[1]. Craig JP, Nichols KK, Akpek EK, et al. TFOS DEWS II definition and classification report. Ocul Surf 2017;15(3):276–83. [PubMed: 28736335]

[2]. Bron AJ, de Paiva CS, Chauhan SK, et al. TFOS DEWS II pathophysiology report. Ocul Surf 2017;15(3):438–510. [PubMed: 28736340]

[3]. Stapleton F, Alves M, Bunya VY, et al. TFOS DEWS II epidemiology report. Ocul Surf 2017;15(3):334–65. [PubMed: 28736337]

[4]. Parfitt GJ, Xie Y, Geyfman M, Brown DJ, Jester JV. Absence of ductal hyperkeratinization in mouse age-related meibomian gland dysfunction (ARMGD). Aging (Albany NY) 2013;5(11):825–34. [PubMed: 24259272]

[5]. Foulks GN, Bron AJ. Meibomian gland dysfunction: a clinical scheme for description, diagnosis, classification, and grading. Ocul Surf 2003;1(3):107–26. [PubMed: 17075643]

[6]. Friedland BR, Fleming CP, Blackie CA, Korb DR. A novel thermodynamic treatment for meibomian gland dysfunction. Curr Eye Res 2011;36(2):79–87. [PubMed: 21281063]

[7]. Dell SJ, Gaster RN, Barbarino SC, Cunningham DN. Prospective evaluation of intense pulsed light and meibomian gland expression efficacy on relieving signs and symptoms of dry eye disease due to meibomian gland dysfunction. Clin Ophthalmol 2017;11:817–27. [PubMed: 28496300]

[8]. Jones L, Downie LE, Korb D, et al. TFOS DEWS II management and therapy report. Ocul Surf 2017;15(3):575–628. [PubMed: 28736343]

[9]. Zhuang-Yan A, Syed YY. Perfluorohexyloctane ophthalmic solution: a review in dry eye disease. Drugs 2024;84(4):441–8. [PubMed: 38554243]

[10]. Saad A, Frings A. Influence of perfluorohexyloctane (Evotears®) on higher order aberrations. Int Ophthalmol 2023;43(12):5025–30. [PubMed: 37864619]

[11]. Jester JV, Rife L, Nii D, Luttrull JK, Wilson L, Smith RE. In vivo biomicroscopy and photography of meibomian glands in a rabbit model of meibomian gland dysfunction. Invest Ophthalmol Vis Sci 1982;22(5):660–7. [PubMed: 7076409]

[12]. Ohnishi Y, Kohno T. Polychlorinated biphenyls poisoning in monkey eye. Invest Ophthalmol Vis Sci 1979;18(9):981–4. [PubMed: 113362]

[13]. Jester JV, Rajagopalan S, Rodrigues M. Meibomian gland changes in the rhino (hrrhhrrh) mouse. Invest Ophthalmol Vis Sci 1988;29(7):1190–4. [PubMed: 2458328]

[14]. Mathers WD, Shields WJ, Sachdev MS, Petroll WM, Jester JV. Meibomian gland morphology and tear osmolarity: changes with Accutane therapy. Cornea 1991;10(4):286–90. [PubMed: 1832371]

[15]. Liu Y, Knop E, Knop N, et al. Growth hormone influence on the morphology and size of the mouse meibomian gland. J Ophthalmol 2016;2016:5728071. [PubMed: 26981277]

[16]. Miyake H, Oda T, Katsuta O, Seno M, Nakamura M. Meibomian gland dysfunction model in hairless mice fed a special diet with limited lipid content. Invest Ophthalmol Vis Sci 2016;57(7):3268–75. [PubMed: 27327582]

[17]. Ibrahim MAA, Elwan WM. Role of topical dehydroepiandrosterone in ameliorating isotretinoin-induced Meibomian gland dysfunction in adult male albino rat. Ann Anat 2017;211:78–87. [PubMed: 28212783]

[18]. Bu J, Wu Y, Cai X, et al. Hyperlipidemia induces meibomian gland dysfunction. Ocul Surf 2019;17(4):777–86. [PubMed: 31201956]

[19]. Ibrahim OM, Dogru M, Matsumoto Y, et al. Oxidative stress induced age dependent meibomian gland dysfunction in Cu, Zn-superoxide dismutase-1 (Sod1) knockout mice. PLoS One 2014;9(7):e99328. [PubMed: 25036096]

[20]. Sassa T, Tadaki M, Kiyonari H, Kihara A. Very long-chain tear film lipids produced by fatty acid elongase ELOVL1 prevent dry eye disease in mice. Faseb J 2018;32(6):2966–78. [PubMed: 29401594]

[21]. Butovich IA, Wilkerson A, Bhat N, McMahon A, Yuksel S. On the pivotal role of Elovl3/ELOVL3 in meibogenesis and ocular physiology of mice. Faseb J 2019;33(9):10034–48. [PubMed: 31208226]

[22]. McMahon A, Lu H, Butovich IA. A role for ELOVL4 in the mouse meibomian gland and sebocyte cell biology. Invest Ophthalmol Vis Sci 2014;55(5):2832–40. [PubMed: 24677106]

[23]. Widjaja-Adhi MAK, Silvaroli JA, Chelstowska S, et al. Deficiency in Acyl-CoA:Wax Alcohol Acyltransferase 2 causes evaporative dry eye disease by abolishing biosynthesis of wax esters. Faseb J : Off publ Fed Am Soc Exp Biol 2020;34(10):13792–808.

[24]. Sawai M, Watanabe K, Tanaka K, et al. Diverse meibum lipids produced by Awat1 and Awat2 are important for stabilizing tear film and protecting the ocular surface. iScience 2021;24(5):102478. [PubMed: 34113821]

[25]. Khanal S, Bai Y, Ngo W, et al. Human meibum and tear film derived cholesteryl and wax esters in meibomian gland dysfunction and tear film structure. Ocul Surf 2022;23:12–23. [PubMed: 34774809]

[26]. Butovich IA. The Meibomian puzzle: combining pieces together. Prog Retin Eye Res 2009;28(6):483–98. [PubMed: 19660571]

[27]. Hisey EA, Martins BC, Donnelly CG, et al. Identification of putative orthologs of clinically relevant antimicrobial peptides in the equine ocular surface and amniotic membrane. Vet Ophthalmol 2023;26(Suppl 1):125–33. Suppl 1. [PubMed: 36478371]

[28]. Eaton JS, Miller PE, Bentley E, Thomasy SM, Murphy CJ. The SPOTS system: an ocular scoring system optimized for use in modern preclinical drug development and Toxicology. J Ocul Pharmacol Therapeut 2017;33(10):718–34.

[29]. Puentes B, Hisey EA, Ferneding M, et al. Development and validation of a method to generate phenol red thread tests. Ocul Surf 2024;34:262–6. [PubMed: 39127389]

[30]. Schmittgen TD, Livak KJ. Analyzing real-time PCR data by the comparative C(T) method. Nat Protoc 2008;3(6):1101–8. [PubMed: 18546601]

[31]. Ruifrok AC, Johnston DA. Quantification of histochemical staining by color deconvolution. Anal Quant Cytol Histol 2001;23(4):291–9. [PubMed: 11531144]

[32]. Arthur D, Vassilvitskii S. k-means++: the advantages of careful seeding. Proceedings of the eighteenth annual ACM-SIAM symposium on Discrete algorithms. New Orleans, Louisiana; 2007.

[33]. Van Uitert R, Bitter I. Subvoxel precise skeletons of volumetric data based on fast marching methods. Med Phys 2007;34(2):627–38. [PubMed: 17388180]

[34]. Butovich IA, Wilkerson A, Yuksel S. Depletion of cholesteryl esters causes meibomian gland dysfunction-like symptoms in a soat1-null mouse model. Int J Mol Sci 2021;22(4).

[35]. Butovich IA, Lu H, McMahon A, et al. Biophysical and morphological evaluation of human normal and dry eye meibum using hot stage polarized light microscopy. Invest Ophthalmol Vis Sci 2014;55(1):87–101. [PubMed: 24282231]

[36]. Yáñez-Soto B, Leonard BC, Raghunathan VK, Abbott NL, Murphy CJ. Effect of stratification on surface properties of corneal epithelial cells. Invest Ophthalmol Vis Sci 2015;56(13):8340–8. [PubMed: 26747762]

[37]. Xie L, Sparks MA, Li W, et al. Quantitative susceptibility mapping of kidney inflammation and fibrosis in type 1 angiotensin receptor-deficient mice. NMR Biomed 2013;26(12):1853–63. [PubMed: 24154952]

[38]. Corrales RM, Narayanan S, Fernández I, et al. Ocular mucin gene expression levels as biomarkers for the diagnosis of dry eye syndrome. Invest Ophthalmol Vis Sci 2011;52(11):8363–9. [PubMed: 21931132]

[39]. Jones DT, Monroy D, Ji Z, Pflugfelder SC. Alterations of ocular surface gene expression in Sjögren's syndrome. Adv Exp Med Biol 1998;438:533–6. [PubMed: 9634933]

[40]. Luo S, Djotyan GP, Joshi R, Juhasz T, Brown DJ, Jester JV. Modeling meibum secretion: alternatives for obstructive meibomian gland dysfunction (MGD). Ocul Surf 2024;31:56–62. [PubMed: 38042297]

[41]. McMahon A, Yuksel S, Bhat N, Pham H, Wilkerson A, Butovich IA. Inactivation of Awat2 in mice causes loss of wax ester lipids from meibum. Invest Ophthalmol Vis Sci 2020;61(7). 2632–2632.

[42]. Enríquez-de-Salamanca A, Castellanos E, Stern ME, et al. Tear cytokine and chemokine analysis and clinical correlations in evaporative-type dry eye disease. Mol Vis 2010;16:862–73. [PubMed: 20508732]

[43]. D'Souza S, Padmanabhan Nair A, Iyappan G, et al. Clinical and molecular outcomes after combined intense pulsed light therapy with low-level light therapy in recalcitrant evaporative dry eye disease with meibomian gland dysfunction. Cornea 2022;41(9):1080–7. [PubMed: 34907942]

[44]. De Paiva CS, Villarreal AL, Corrales RM, et al. Dry eye–induced conjunctival epithelial squamous metaplasia is modulated by interferon-γ. Invest Ophthalmol Vis Sci 2007;48(6):2553–60. [PubMed: 17525184]

[45]. Matsumoto Y, Ibrahim OMA, Kojima T, Dogru M, Shimazaki J, Tsubota K. Corneal in vivo laser-scanning confocal microscopy findings in dry eye patients with sjögren's syndrome. Diagnostics 2020;10(7).

[46]. Zhang J, Yan X, Li H. Analysis of the correlations of mucins, inflammatory markers, and clinical tests in dry eye. Cornea 2013;32(7):928–32. [PubMed: 23538614]

[47]. Bhatt K, Singh S, Singh K, Kumar S, Dwivedi K. Prevalence of dry eye, its categorization (Dry Eye Workshop II), and pathological correlation: a tertiary care study. Indian J Ophthalmol 2023;71(4):1454–8. [PubMed: 37026281]

[48]. Mantelli F, Argüeso P. Functions of ocular surface mucins in health and disease. Curr Opin Allergy Clin Immunol 2008;8(5):477–83. [PubMed: 18769205]

[49]. Argüeso P, Gipson IK. Epithelial mucins of the ocular surface: structure, biosynthesis and function. Exp Eye Res 2001;73(3):281–9. [PubMed: 11520103]

[50]. Nagar S, Ajouz L, Nichols KK, et al. Relationship between human meibum lipid composition and the severity of meibomian gland dysfunction: a spectroscopic analysis. Invest Ophthalmol Vis Sci 2023;64(10):22.

[51]. Borchman D, Ramasubramanian A, Foulks GN. Human meibum cholesteryl and wax ester variability with age, sex, and meibomian gland dysfunction. Invest Ophthalmol Vis Sci 2019;60(6):2286–93. [PubMed: 31112994]

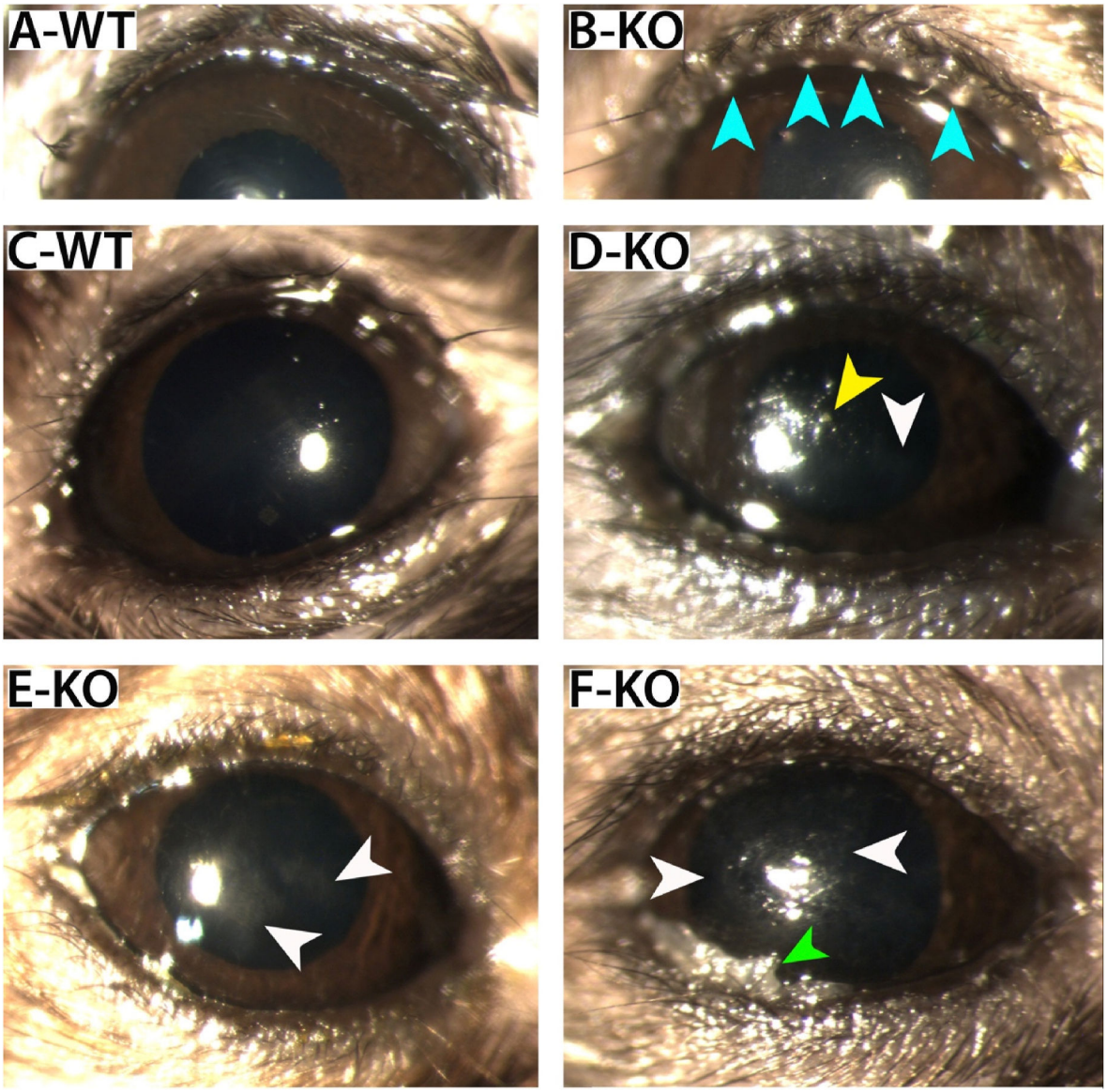

Fig. 1. Slit lamp biomicroscopy reveals inspissated meibomian gland orifices and corneal opacities in *Awat2* KO mice.

Slit lamp biomicroscopy image analysis identified that WT mice had normal eyelid margins (A), while the *Awat2* KO mice exhibited meibomian gland orifices that are obstructed with white material (blue arrows, B). Additionally, the WT mice (C) had clear corneas whereas the *Awat2* KO mice (D–F) exhibited mild to moderately dense corneal lesions (white arrows). Several of the *Awat2* KO mice had white material present on their ocular surface (yellow arrow, D) or adherent to their eyelid margin (green arrow, F), highlighting the inability of this altered meibum to incorporate into the tear film normally.

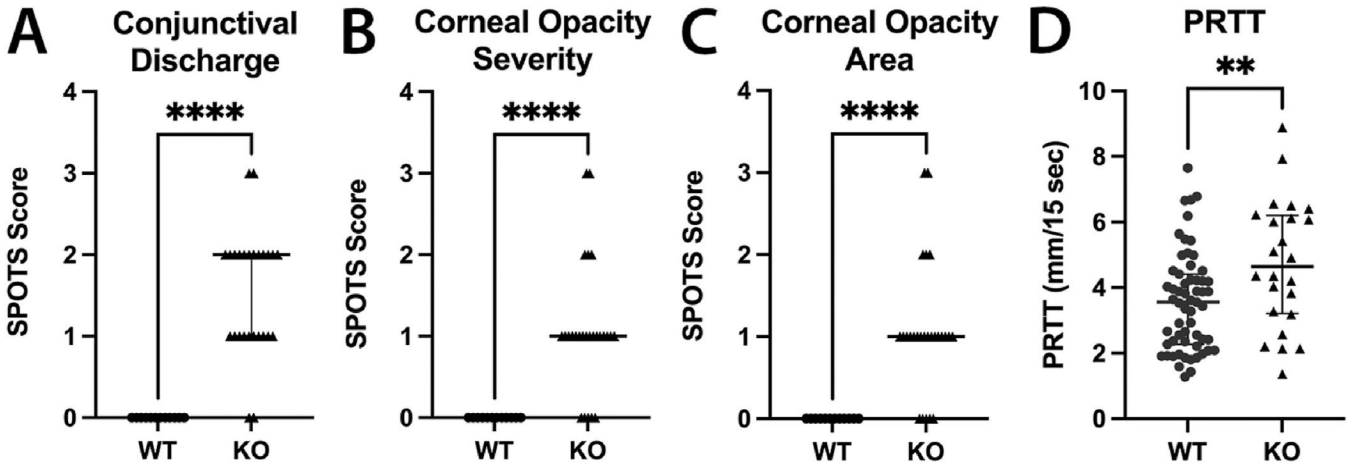

Fig. 2. SPOTS scores and PRTT measurements of *Awat2* KO and WT mice demonstrate increased corneal pathology of *Awat2* KO eyes.

A Mann-Whitney test identified a significant increase in conjunctival discharge (used to denote meibum along the eyelid margin, A), corneal opacity severity (B) and corneal opacity area (C) in the *Awat2* KO (n = 13, triangles) mice compared to the WT mice (n = 6, circles, $P < 0.0001$), suggesting that the lack of *Awat2* induces clinically detectable ocular surface and adnexal pathology by six months of age. The aqueous tear volume of two-month-old *Awat2* KO (n = 6) and WT (n = 10) was determined using the phenol red thread test (PRTT, D). The thread was placed under the eyelid margin of awake animals adjacent to the lateral canthus for 15 s, then the color change was measured with digital calipers. The *Awat2* KO mice were tested twice and the WT mice three times with at least a 24-h recovery period between experiments. A Mann-Whitney test was utilized to compare the PRTT measurements, which identified a significant increase in tear volume in the *Awat2* KO mice compared to the WT controls as shown previously ($P = 0.0098$) [29]. These findings suggest that there is a compensatory increase in aqueous tear production due to the altered meibum lipid composition of these mice. Data presented are the median and interquartile range.

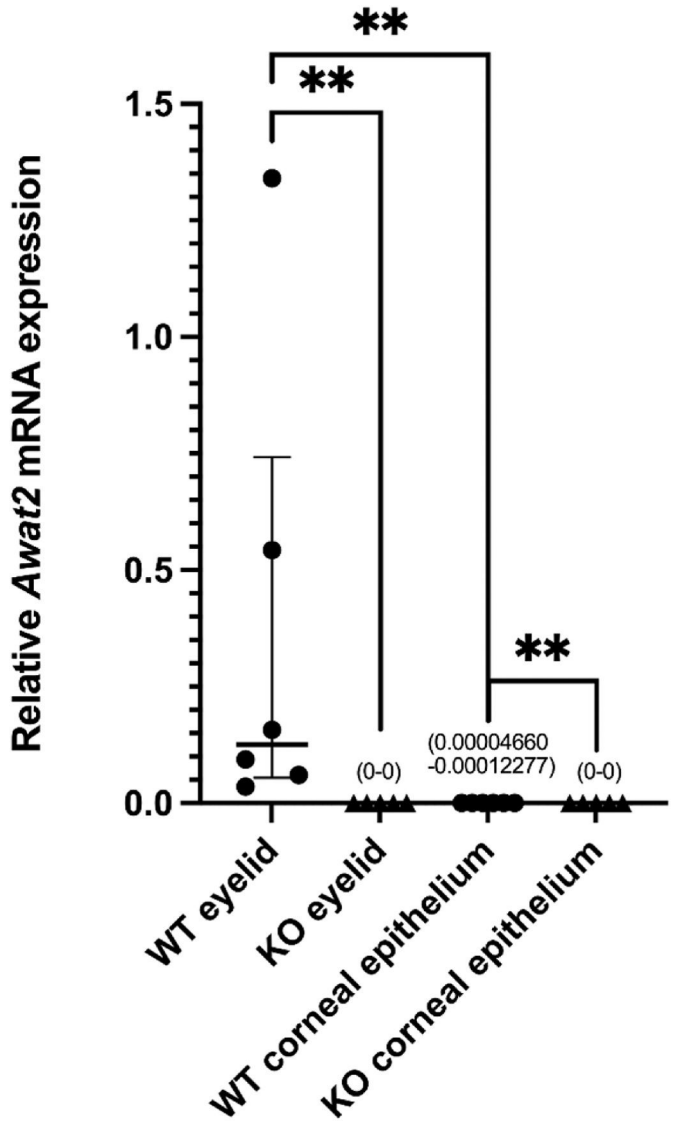

Fig. 3. qPCR of the meibomian glands and corneal epithelium of *Awat2* KO mice identified complete loss of *Awat2* expression.

The relative expression of *Awat2* was determined by utilizing the $2^{-\Delta Ct}$ method to normalize the Ct values to the *Gapdh* expression. A Mann-Whitney test was utilized to compare the *Awat2* expression of the *Awat2* KO (n = 5, triangles) and WT (n = 6, circles) meibomian gland and corneal epithelium, which identified a significant decrease in *Awat2* expression in the meibomian glands and corneal epithelium of *Awat2* KO mice ($P = 0.0043$). A Mann-Whitney test was also utilized to compare the *Awat2* expression between the meibomian glands and the corneal epithelium of WT mice, which identified a significantly lower *Awat2* expression in the corneal epithelium of WT mice ($P = 0.0022$). This negligible expression of *Awat2* identified in the corneal epithelial samples indicates that the corneal phenotype is likely secondary to the altered tear film rather than the direct effect of the loss of *Awat2* on the corneal epithelial cells. Data presented are median and interquartile ranges, numbers in parenthesis indicate the range in $2^{-\Delta Ct}$ values for that group.

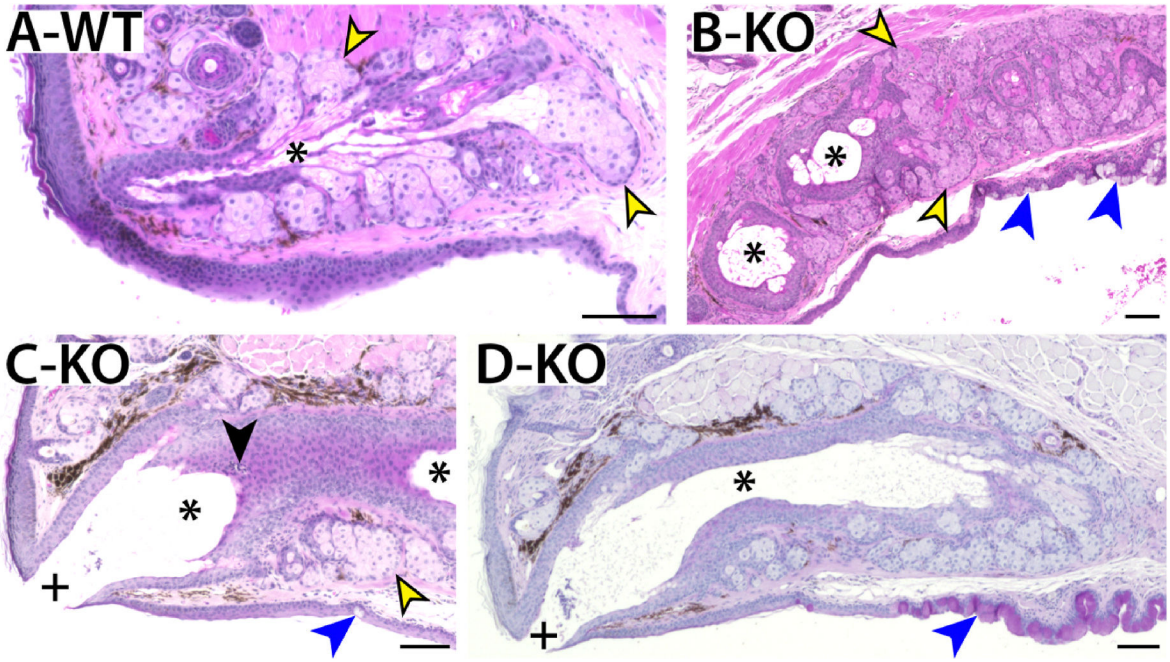

Fig. 4. Meibomian ductal hyperplasia and dilated orifices and central ducts identified in the *Awat2* KO eyelids.

Eyelids were collected from 9- and 18-month-old mice post-mortem, fixed with paraformaldehyde, paraffin-embedded, and stained with H&E. The WT section (A) exemplifies the normal arborous morphology of the meibomian gland with acinar tissue (yellow arrows) connected to ductules, which converge to form the central duct (*) leading to the meibomian gland orifice (not present in this section). All *Awat2* KO (B and C) meibomian glands have dilated central ducts (*) and orifices (+) in addition to ductal epithelial hyperplasia. Inflammatory cell infiltration (black arrow) is present in the meibomian gland lumen and surrounding the central duct in some *Awat2* KO sections, which is not present in the WT sections. In addition, goblet cells (blue arrows) are visible in the conjunctival epithelium of the *Awat2* KO sections, but not in the WT tissues. Periodic acid-Schiff staining was performed to confirm the identify of these cells (D, from the same tissue sample as image C). Scale bars: 100 μm, A–C: 10X magnification, D: 4× magnification.

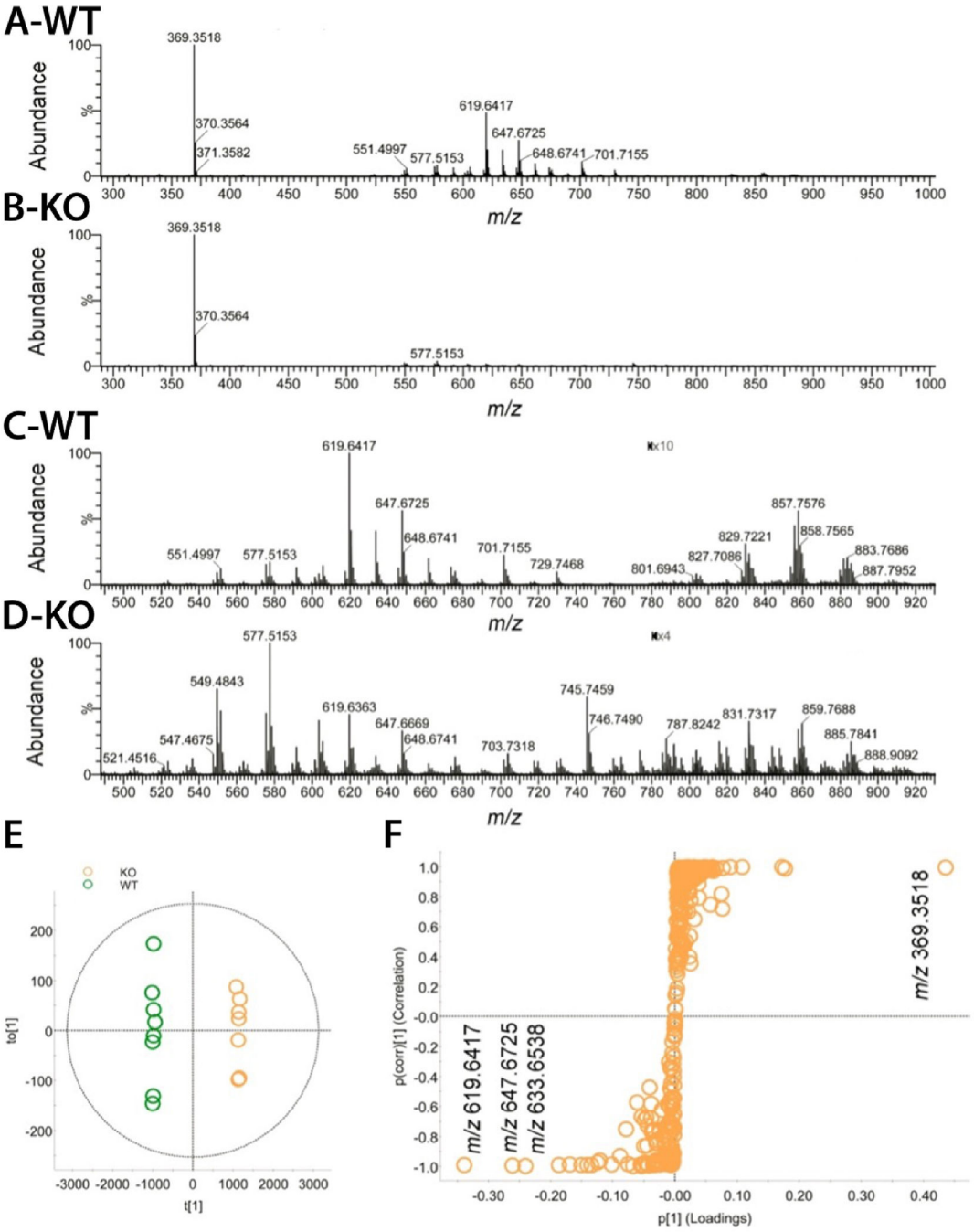

Fig. 5. Lipidomic analyses of *Awat2* KO meibomian lipids using LC-MS identifies significant decrease in wax esters and an increase in cholesteryl esters.

The WT and *Awat2* KO meibum were analyzed in atmospheric pressure chemical ionization positive ion mode (APCI PIM). Observation spectra of two representative WT (A) and *Awat2* KO (B) samples with expanded sections of the WT (C) and *Awat2* KO (D) spectra are shown here. A scores plot of the WT and *Awat2* KO meibum samples was obtained using an untargeted OPLS-DA analysis, highlighting the similarities in the meibum samples between experimental animals with the same genotype and the major differences between the two genotypes (E). A S-Plot of the study samples was also generated with the most

influential lipid analytes occurring in the lower left (wax esters) and the upper right quadrants (cholesteryl esters, F).

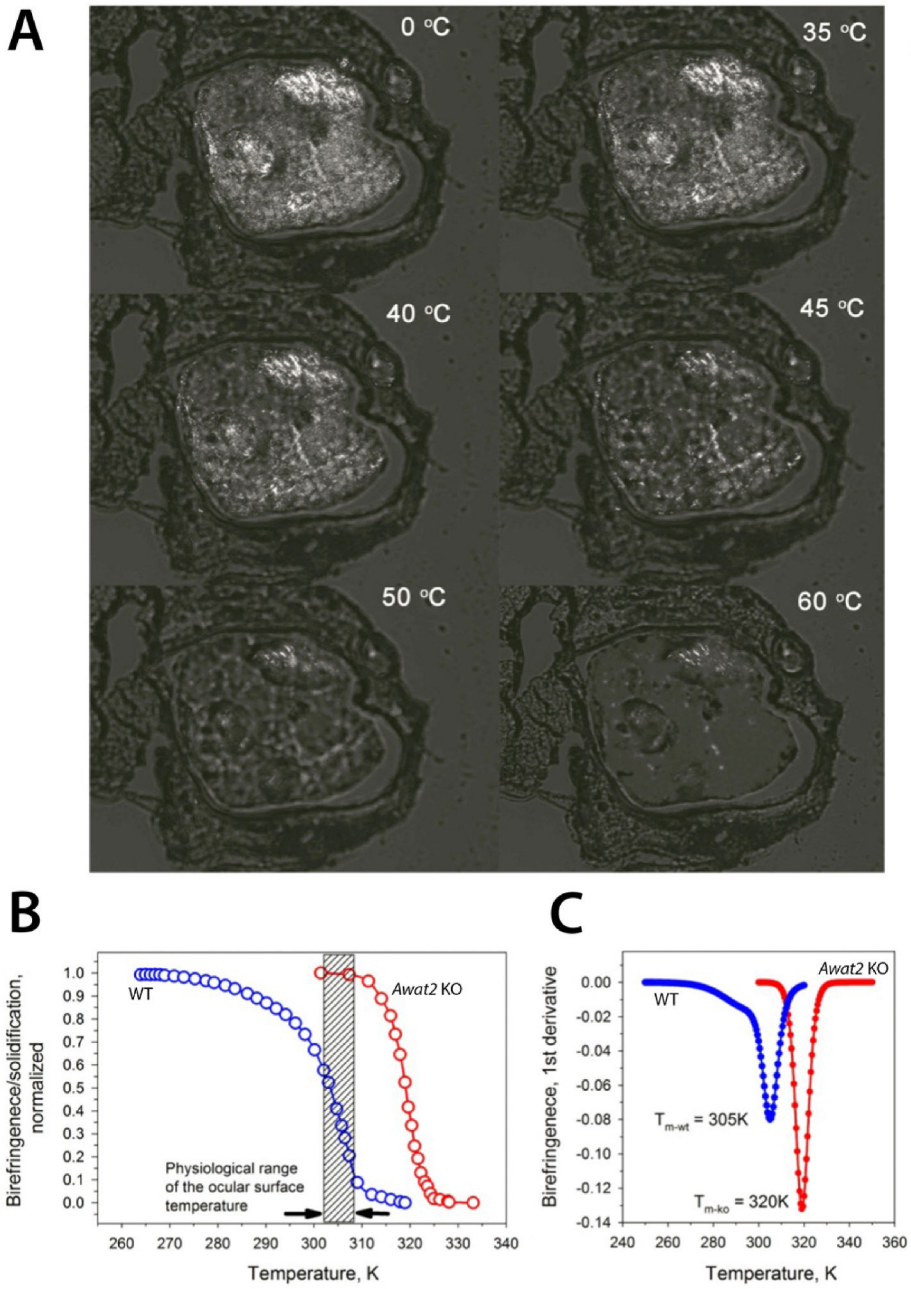

Fig. 6. Thermotropic transitions in WT and *Awat2* KO mouse meibum indicate an increased melting temperature of *Awat2* KO meibum.

Melting characteristics of meibum in 10 μm cryosections of murine meibomian glands were investigated using heat stage cross-polarized light microscopy [34,35]. Representative images of an *Awat2* KO tarsal plate are shown at different temperatures (A), highlighting the temperature-dependent changes in birefringence. Melting curves were generated for the tissue sections to determine the main transition temperatures (T_m) of the samples (B), which were then numerically differentiated to more precisely determine the transition temperature (C).

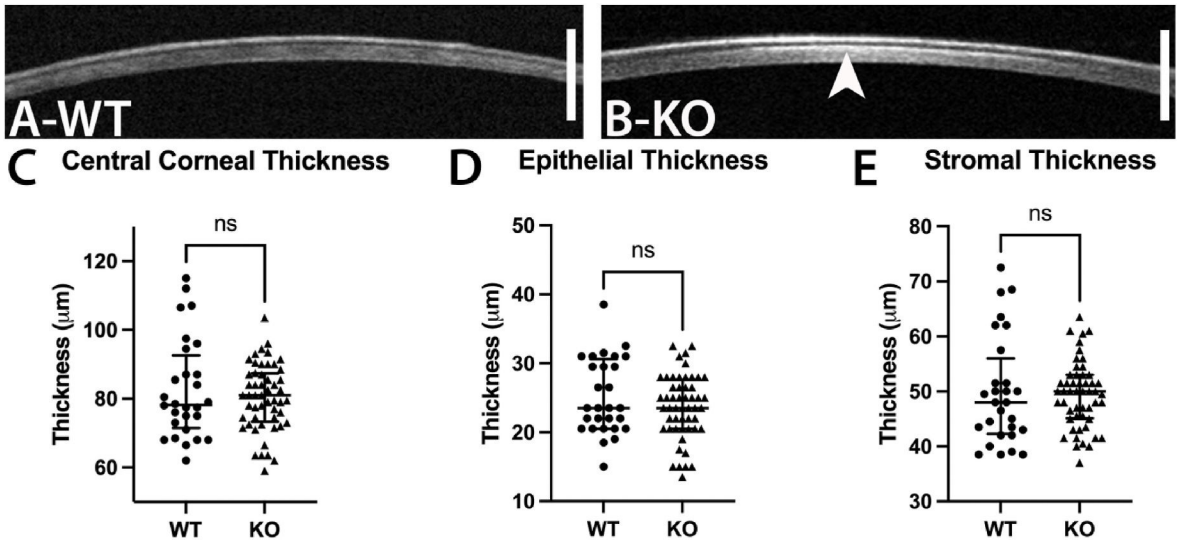

Fig. 7. OCT image analysis of *Awat2* KO and WT mice identified hyperreflectivity of the *Awat2* KO anterior stroma but no difference in thickness measurements.

OCT images were taken of six-month-old WT (A) and *Awat2* KO mice (B), which a identified a hyperreflective stroma in the *Awat2* KO mice (white arrow). The hyperreflective character was indicative of fibrosis present in the anterior stroma. In addition, the central corneal, epithelial, and stromal thicknesses were measured. A Mann-Whitney test was performed to compare the OCT measurements from WT (n = 14, circles) and *Awat2* KO (n = 26, triangles) mice, which identified no significant differences in central corneal (C), epithelial (D), or stromal (E) thickness between the *Awat2* KO and WT mice ($P > 0.05$). These results indicate that mild corneal disease is present in these mice that did not induce a change in corneal thickness. Data presented are median and interquartile range. Scale bars: 250 μm.

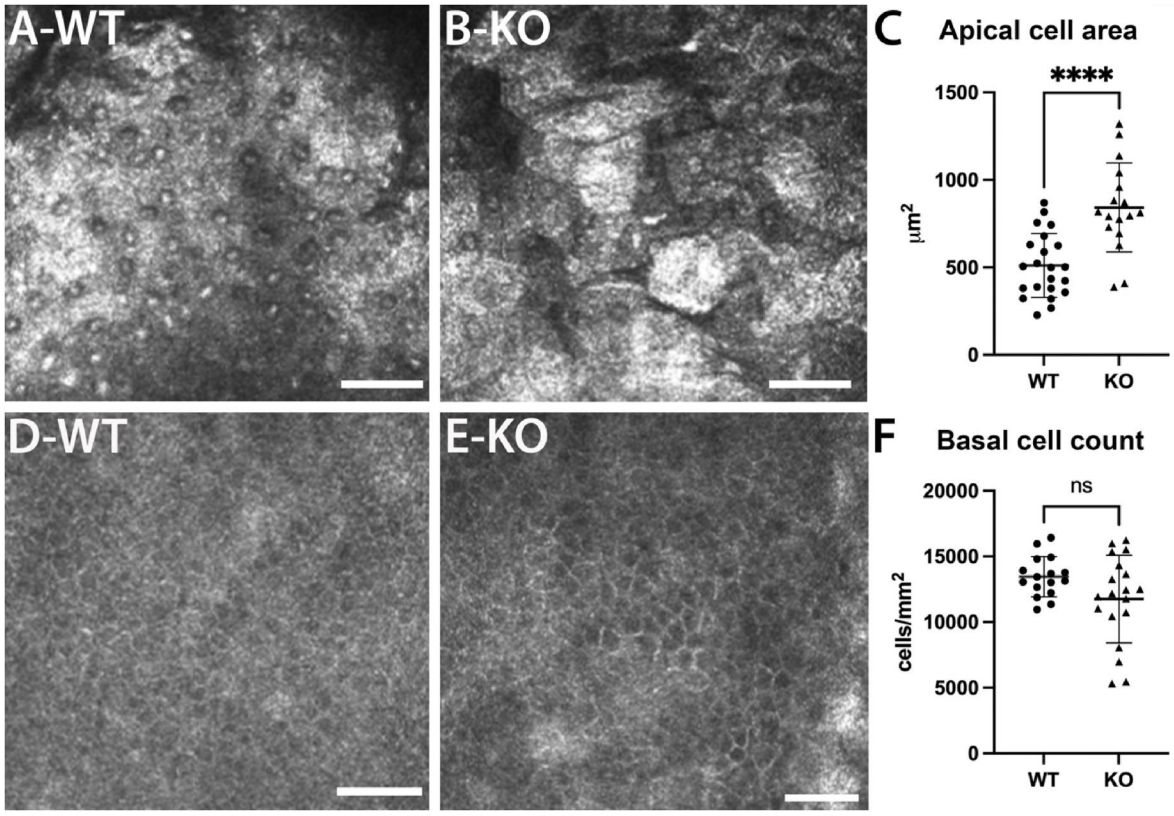

Fig. 8. IVCM analysis identified increased hyperreflectivity and size of apical epithelial cells of *Awat2* KO corneas.

IVCM was performed on six-month-old WT (A and D) and KO (B and E) mice, which identified that the *Awat2* KO apical epithelial cells (B) were hyperreflective with larger spaces between the cells compared to the WT epithelia (A). Additionally, the apical epithelial cells present appeared to be larger in the *Awat2* KO corneas. To quantify this finding, the apical cell area was measured for 5–7 apical epithelial cells from a single image, which identified a significant increase in apical epithelial cell area in the *Awat2* KO corneas (C, $P < 0.0001$). The basal epithelial cells also appeared larger. However, when the basal cell density was compared between the *Awat2* KO (E) and WT mice (D), there was a trend towards a decrease in the *Awat2* KO mice, but this difference was not significant (F, $P = 0.0693$). This increase in cell size and identification of regions without apical epithelial cells indicate that there is an increased loss of epithelial cells in the *Awat2* KO mice, indicative of ocular surface disease that recapitulates the increase in superficial epithelial cell area seen in human patients with dry eye [45]. Data presented are mean and standard deviation. Scale bars: 50 µm.

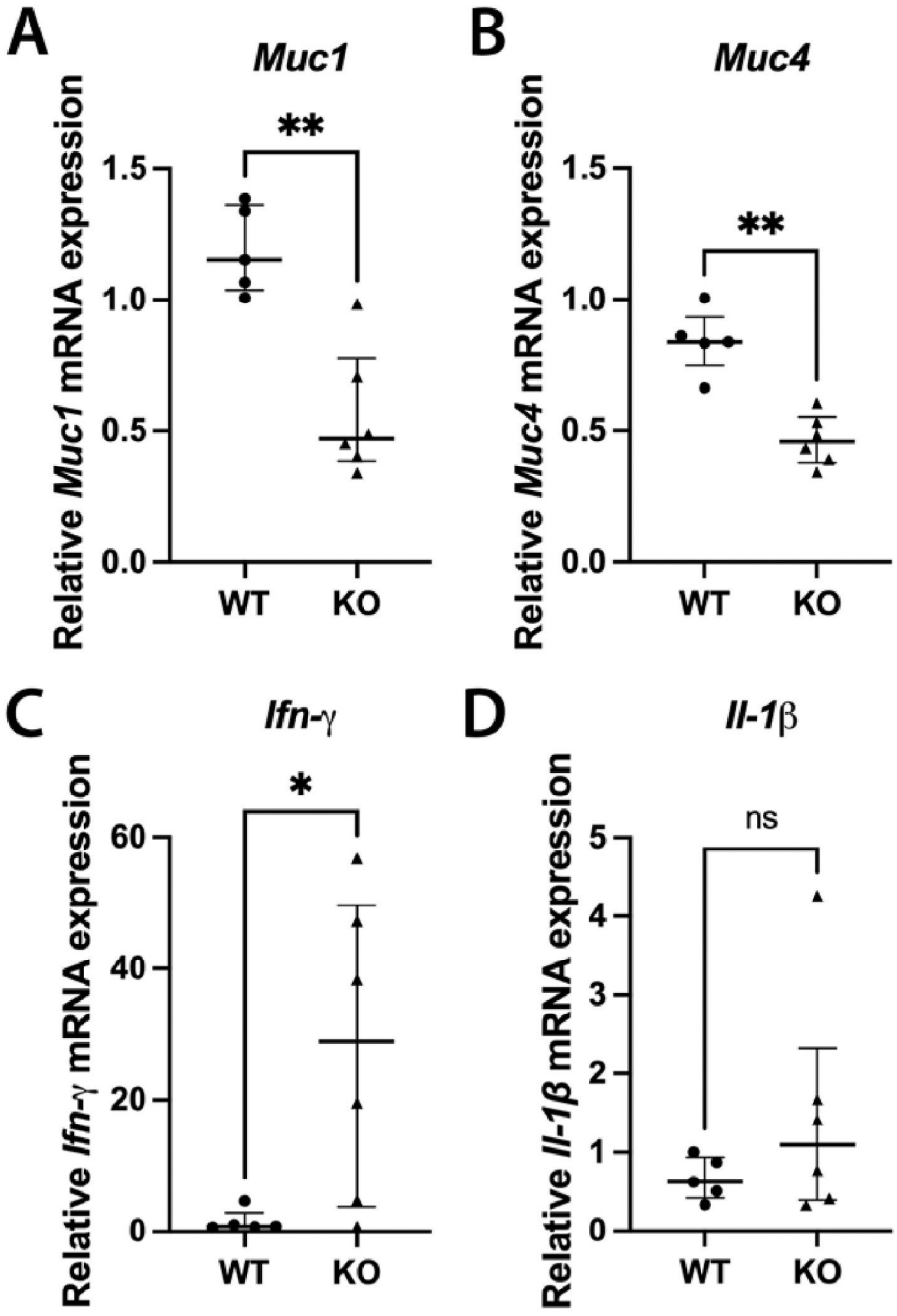

Fig. 9. qPCR of the corneal epithelium of *Awat2* KO mice identified altered mucin and inflammatory cytokine expression.

The relative expression of each gene was determined by utilizing the $2^{-\Delta Ct}$ method to normalize the Ct values to *Gapdh* expression. A Mann-Whitney test was utilized to compare the qPCR results of the *Awat2* KO (n = 6, triangles) and WT (n = 5, circles) corneal epithelium, which identified a significant decrease in *Muc1* ($P = 0.0043$) and *Muc4* ($P = 0.0043$) expression and a significant increase in *Ifn-γ* expression ($P = 0.0303$). However, no difference in *Il-1β* expression was identified ($P = 0.5368$). These results indicate that ocular surface inflammation is present, which could lead to the downregulation of mucin

expression, a phenomenon seen in human patients with DED [38,39]. Data presented are median and interquartile ranges.

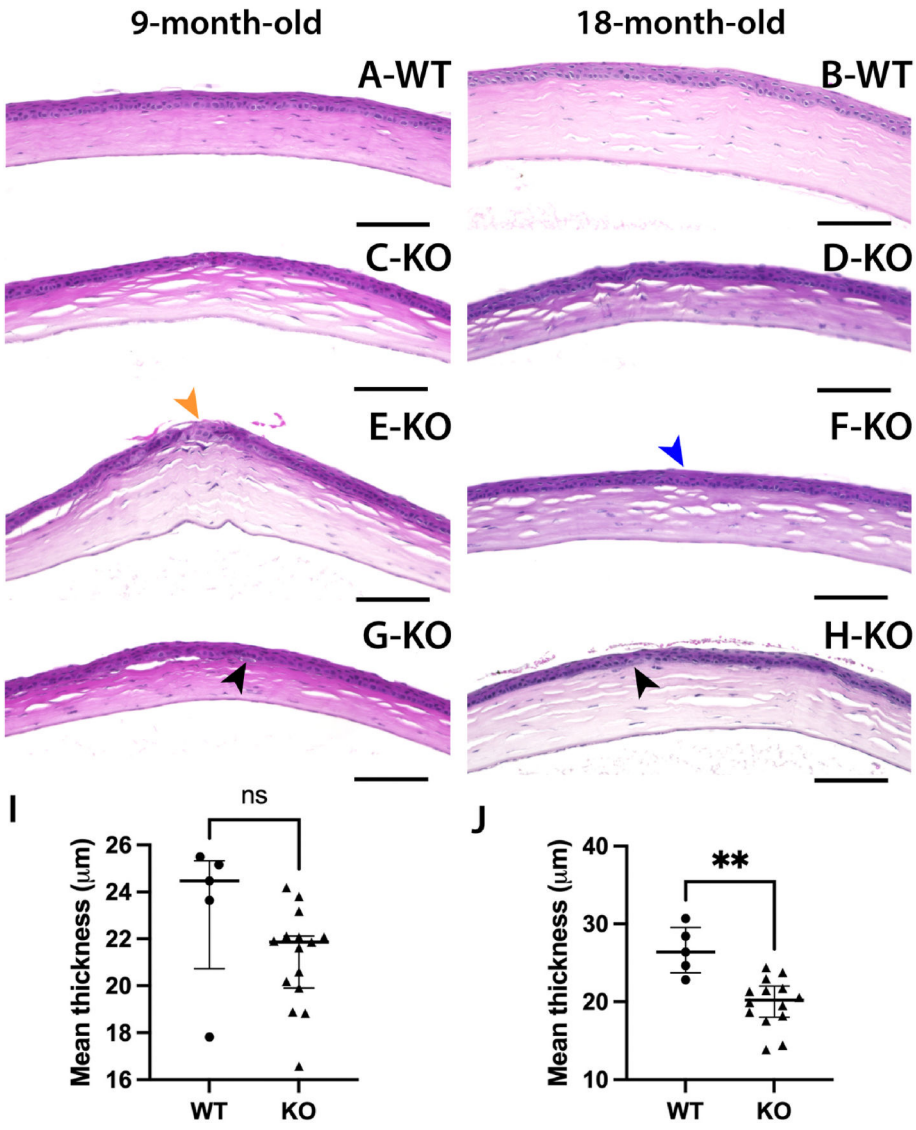

Fig. 10. Similar pathologies identified in *Awat2* KO corneas at 9 months and 18 months of age.

Globes were enucleated from 9-month-old and 18-month-old mice post-mortem, fixed with paraformaldehyde, paraffin-embedded, and stained with hematoxylin and eosin. The WT corneas at 9 months (A) and 18 months (B) are both normal. The *Awat2* KO corneas (C–H) have mild pathologies. The anterior stroma of *Awat2* KO corneas was hypereosinophilic at 9 (C) and 18 months (D). Epithelial degeneration (E, orange arrow) and disorganization (F, blue arrow) were also identified at 9 and 18 months, respectively. Basophilic subepithelial deposits (black arrows) were identified in a few corneas at 9 (G) and 18 months (H) as well. Scale bars: 100 μm, 20X magnification. The thickness of the corneal epithelium was determined using a custom MATLAB script. When the corneal epithelial thickness was compared between the WT and the *Awat2* KO corneas, a trend towards a decrease in corneal epithelial thickness was identified in the 9-month-old *Awat2* KO corneas (Mann-Whitney, $P = 0.0655$, I) and a significant decrease in corneal epithelial thickness was identified in the 18-month-old *Awat2* KO corneas (Mann-Whitney, $P = 0.0012$, J).

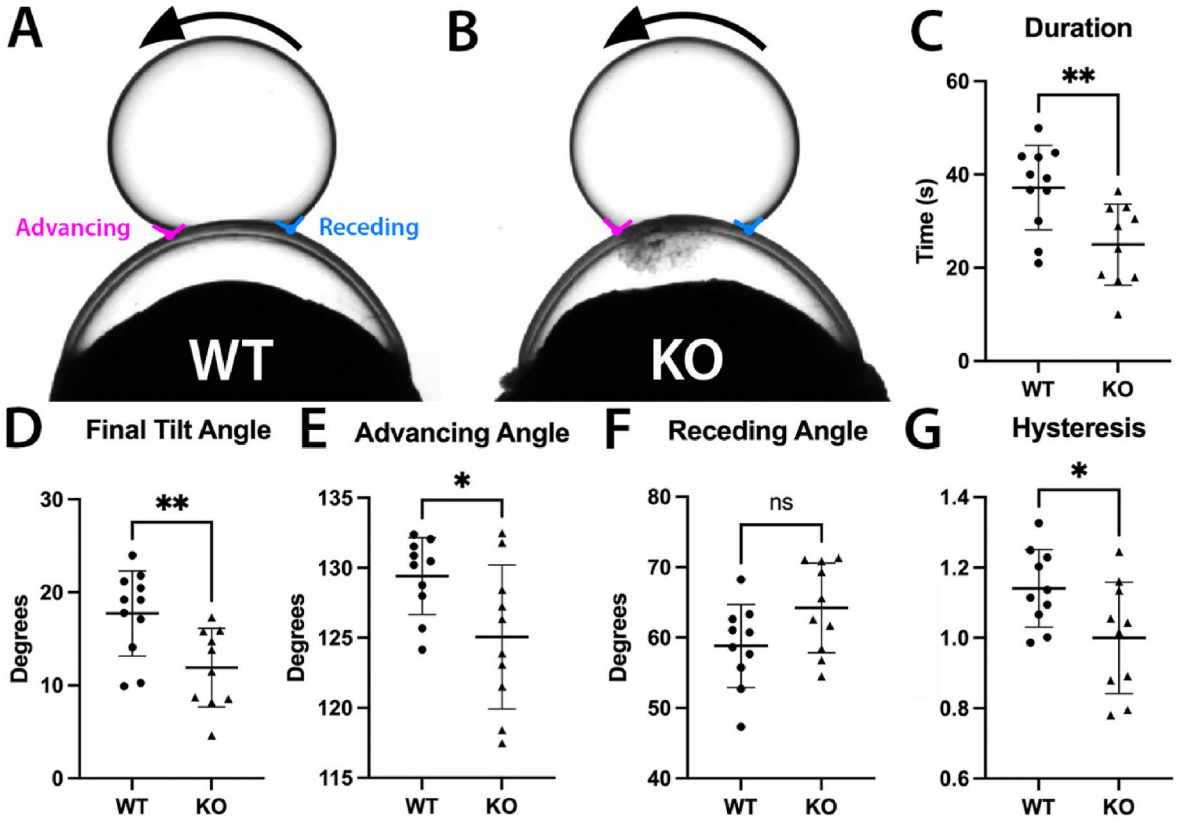

Fig. 11. Dynamic contact angle goniometry analysis identified decreased droplet adherence to the *Awat2* KO ocular surface.

A five μL droplet of perfluorodecalin was placed on the axial cornea of a globe adhered to a glass slide. The slide was placed in a dynamic contact angle goniometer and tilted until the droplet was dislodged. On visualization of the globes, half of the *Awat2* KO corneas assessed had a lesion on the ocular surface (A) compared to the healthy ocular surface of all WT globes (B). The advancing angle is depicted in pink and the receding angle is shown in blue. A student's *t*-test was performed to compare the average measurements of three videos from *Awat2* KO (n = 10, triangles) and WT (n = 11, circles) globes for the duration of droplet contact (C), the final tilt angle of system (D), the advancing angle (E), the receding angle (F), and the hysteresis (G). There was a significant decrease in the duration ($P = 0.0053$) and the final tilt angle ($P = 0.0072$) in the *Awat2* KO globes, suggesting that there is a decreased ability of the *Awat2* KO globes to adhere the droplet to the ocular surface, and therefore the tear film to the ocular surface. A significant decrease in the advancing angle was identified in the *Awat2* KO globes ($P = 0.0299$), which lead to a significant decrease in the hysteresis value as well ($P = 0.0331$). Additionally, there was a trend towards a significant increase identified in the receding angle ($P = 0.0637$). Data shown represent mean and standard deviation.